Metal−Organic Framework−Polyacrylonitrile Composite Beads for Xenon Capture

Brian J. Riley, Saehwa Chong, Wenbin Kuang, Tamas Varga, Ahmed S. Helal, Mitchell Galanek, Ju Li, Zayne J. Nelson, and Praveen K. Thallapally*

Read Online

ACCESS | Metrics & More | Article Recommendations | Supporting Information

ABSTRACT: Mechanically robust forms of HKUST-1 metal−organic frameworks (MOFs) were fabricated by embedding the MOF crystals in a passive polyacrylonitrile (PAN) matrix at different MOF loadings of 10−90 mass %. PAN is highly porous and acts as a scaffold that holds the active MOF adsorbent in place. These MOF−PAN composites were then evaluated for capturing Xe. Data presented herein show that the PAN matrix does not notably interfere with the Xe capture process, where the Xe capacities scale somewhat linearly with the increase in MOF loadings within the composites. Also, γ radiation exposures to the composites revealed that they are highly tolerant to these types of radiation fields.
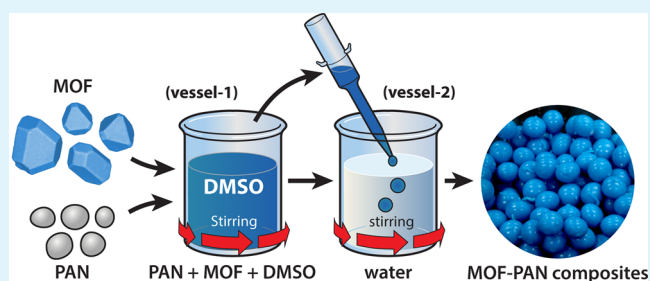
1. INTRODUCTION

During aqueous processing of used nuclear fuel, four volatile radionuclides (^3H, ^{14}C, Kr, and ^{129}I) are released and novel materials are required for their capture.[1] Although Xe is generated as a fission product, by the time the fuel would likely be reprocessed, all of the radioactive isotopes would have decayed to negligible quantities.[1−3] Nevertheless, nonradioactive Xe is present at a 10× higher concentration than the total Kr content and poses issues for capturing Kr amongst Xe, considering that they both are noble gases and require similar capture processes. Given the higher polarizability of Xe over Kr,[4] the majority of adsorbent materials capture Xe selectively over Kr. For waste management to be efficient, the process should also separate Xe from the captured Kr. Further capturing nonradioactive Xe from reprocessing facilities provides economic incentives because high-purity Xe has numerous applications such as in the medical industry for anesthesia, in the space industry as a propellant, and in the automobile industry for high-output headlamps.[5−8]

The most mature process used to remove noble gases is cryogenic distillation.[9] In this process, off-gases are first cleaned to remove H_2O, O_2, NO_x, and CO_2. Then, the resulting gas is cooled to liquid N_2 temperature (77 K) where Xe and Kr are solids. However, at the low concentrations in the process off-gas streams, Xe and Kr are dissolved in the liquid N_2 and can be separated from N_2 by cryogenic distillation, leaving behind a mixture of Xe and Kr (and possibly Ar) that can be further divided with a sufficiently large distillation apparatus. Installing and operating a cryogenic process can be

very expensive and energy-intensive. Thus, a process in which Xe removal could be performed at much higher temperatures would be advantageous and cost-effective, especially if the process could be operated close to ambient conditions and the adsorbent materials used in the process are cost competitive.

In this regard, a large number of solid sorbents have been evaluated for the selective removal of these noble gases at room temperature with a composition that is representative of conditions to be expected during nuclear fuel reprocessing including metal−organic frameworks (MOFs), covalent organic frameworks (COFs), zeolites, and membranes.[10−12] Among all of the materials tested, MOFs have shown to be a very promising class of materials because the pore size, pore shape, and specific surface area can be manipulated with the choice of organic building blocks and metal clusters.[13,14] Given the high polarizability of Xe, most MOFs tested were selective toward Xe over other noble gases. Based on our experimental observations, several factors influence the selectivity of weakly interacting gases within MOFs. For example, MOFs with unsaturated open metal sites offer stronger adsorbate−MOF interactions; however, these adsorbents are not selective for noble gases when other competing gases such as H_2O and CO_2
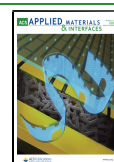
are present.[15−18] Similarly, other MOF attributes studied include ligand polarizability, hydrophilic and hydrophobic surface functionalities, surface area, pore size, presence of metal nanoparticles, and temperature.[19−27] Overall, all of these factors play a significant role in the ability of these materials to separate noble gases from each other and from air.[28−31]

Given the large diversity of MOFs, computational approaches were developed to identify the MOFs with the highest Xe uptake and selectivity at room temperature using experimental and hypothetical databases.[32−34] For example, the CaSDB MOF is one of the successful MOFs identified as Xe-selective by molecular simulations in a database containing 5000 experimental and 125 000 hypothetical MOFs.[10,35] The computational prediction was confirmed by conducting laboratory experiments that showed the highest Xe/Kr selectivity of 16 in the presence of other gases including CO_2 and humidity (i.e., 400 ppm Xe, 40 ppm Kr, balanced with air).

Although several materials were shown to be very promising, one fundamental issue impeding large-scale deployment of MOFs in commercial and industrial applications is the high pulverulent properties. That is, MOFs tend to be mechanically fragile and sticky, and loose powders can be easily entrained in flowing gas streams as an aerosol. Thus, the shaping of MOFs on a macroscopic level, such as converting a fine microcrystalline powder into a shaped body while simultaneously preserving the intrinsic adsorbent properties of the MOF, is essential for successful deployment of these materials.[36,37] Strategies to overcome this problem involve the evaluation of various binders and processes to produce MOFs with different shapes including pressing, extrusion, and granulation to produce pellets, granules, and spheres.[38] In general, shaping of adsorbents for off-gas processes improves handling and reduces the pressure drop for flow-through systems. Several industries produce shaped bodies of various adsorbent materials (e.g., zeolites) for applications in catalysis, separation, and adsorption. With spherical granules, fluidized bed reactors could be implemented, where adsorbent macrobeads are moved in and out of a vessel by granular flow. This obviously puts a requirement on the mechanical robustness and wear-resistance of the engineered beads without sacrificing too much of the superior adsorbent properties of the MOFs.

In this regard, the current study was focused on developing mechanically robust, spherically shaped MOF−polyacrylonitrile (PAN)-based composites for the first time using a technique described previously that was developed through a joint collaboration with Idaho National Laboratory.[39,40] To demonstrate the MOF−PAN composite, efforts were focused on a commercially available MOF known as HKUST-1. Several composites were fabricated with different MOF/PAN ratios ranging from 10 to 90 mass % HKUST-1. Several modifications to the previous work were made to optimize the PAN composites for the HKUST-1 MOF.

2. MATERIALS AND METHODS

2.1. Metal−Organic Framework (HKUST-1). For these experiments, the HKUST-1 metal−organic framework (MOF) was acquired commercially from Sigma-Aldrich (688614-100G) and was produced by BASF. Synonyms for this material include copper benzene-1,3,5-tricarboxylate, Cu-BTC, or MOF-199. The term HKUST refers to the location where it was discovered, i.e., Hong Kong University of Science and Technology.

2.2. Composite Fabrication. A high-level graphic depicting the composite synthesis process is shown in Figure 1, and the synthesis
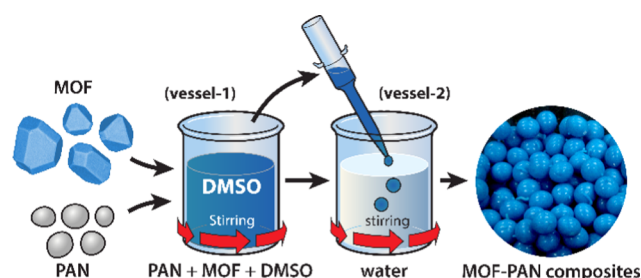

Figure 1. Schematic showing the general process used to make the PAN−MOF composites. See the text for definitions of abbreviations.

details can be found in Table 1. First, PAN fibers (X100, 3.3 dtex, 60 mm; Dralon GmbH, Dormagen, Germany) were dissolved in

Table 1. HKUST-1/PAN Composite Sample Synthesis Details, i.e., m_{PAN}, V_{DMSO}, $m_{HKUST-1}$, and T_{DIW} Denote the Mass of PAN Fibers Added, the Volume of DMSO, the Mass of HKUST-1 MOF Added, and the Temperature of the DIW Bath to Which the Drops Were Added to Create Beads, Respectively

sample ID	m_{PAN} (g)	V_{DMSO} (mL)	$m_{HKUST-1}$ (g)	T_{DIW} (°C)
0%HK	0.2002	3.0		4.5
10%HK	0.2007	3.0	0.0222	4.3
25%HK	0.2002	3.0	0.0664	4.8
75%HK	0.2012	3.0	0.5998	5.3
90%HK	0.1335	2.0	1.2006	3.2

dimethyl sulfoxide (DMSO, Sigma-Aldrich, ≥99.9%) at a ratio of 1:15 (g PAN mL^{-1} DMSO) inside a 20 mL glass scintillation vial. Once the PAN fibers were visibly dissolved in the DMSO ($t < 30$ min), the proper amount of MOF was added to the mixture and suspended. Quickly thereafter ($t < 5$ min), the solution was pipetted out and added to a 5 mL pipette tip suspended ∼5 cm above a dish containing ∼100 mL of deionized water (DIW; 18.2 MΩ·cm) stirring on a stir plate with a Teflon-coated magnetic stir bar; the droplets were slowly added to the DIW. (Note: at this point, it is important not to allow the new droplets to hit the droplets already inside the dish or they will connect with one another.) Once the entire solution was formed into droplets, the solution containing the composites was mixed vigorously for 5 min, at which point the DIW was removed and replaced with fresh DIW; this process was conducted at least three separate times to allow time for the DMSO to be removed from the composites through passive diffusion into the surrounding DIW. Due to the water sensitivity of HKUST-1, this contact time with the DIW was minimized as much as possible. Following the final soak, the beads were removed from the solution, added to a new (pretared) 20 mL scintillation vial, and placed inside a vacuum oven at 150 °C to dry to constant mass under house vacuum.

2.3. Imaging of Composites: Optical and Scanning Electron Microscopies. For optical microscopy, samples were mounted in resin for cross-sectional viewing. First, two composite beds from each loading were added to separate 1.5 mL Eppendorf centrifuge tubes and ∼1 mL of LR White (hard grade, Electron Microscopy Sciences, Hatfield, PA). These were cured in an oven at 60 °C overnight. Then, these were mounted within resin (Allied High Tech) in a single 2″ puck and polished using glycol-based diamond suspensions to a 0.25 μm finish. Optical micrographs were captured with a Leica MZ12$_5$ microscope using a ProgRes SpeedXT^{core} 5 camera (Jenoptik, Jena, Germany) or a Keyence VHX-2000 microscope. Images were postprocessed in Adobe Photoshop CC 2019 to adjust for color accuracy, brightness, and contrast.

The activated HKUST-1 MOF (150 °C overnight in a vacuum oven) as well as the composites were analyzed with a JSM-7001F field-emission gun microscope (JEOL USA, Inc.; Peabody, MA)
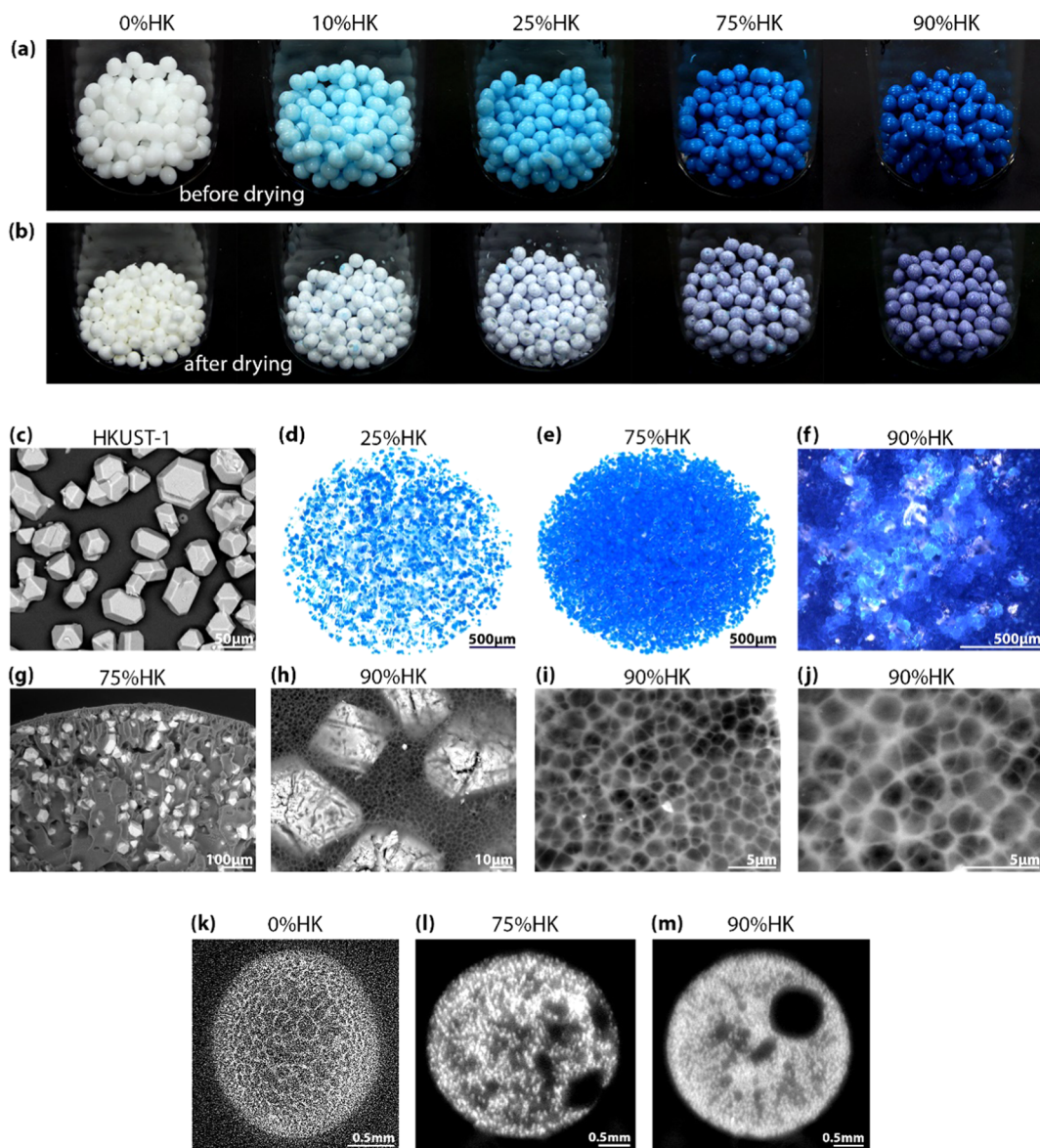
Figure 2. (a, b) Pictures of the MOF−PAN composites as a function of MOF loading in mass % (a) before drying and (b) after drying. (c−j) SEM and OM collage of (c) activated HKUST-1 MOF (HV-SEM-BSE) micrographs and (d−j) MOF−PAN composites including (d−f) cross-sectional views of (d) 25%HK, (e) 75%HK, and (f) 90%HK and (g−j) LV-SEM-BSE micrographs of (g) the inside of a cut 75%HK bead and (h−j) the outside of a 90%HK bead showing the HKUST-1 crystals within the polymer matrix as well as (i, j) higher-resolution views of the polymer web-type matrix on the outside of a 90%HK bead. (k−m) XCT images including (k) 0%HK (100%PAN), (l) 75%HK, and (m) 90%HK.

operated in high-vacuum mode using a backscatter detector (HV-SEM−BSE) or in low-vacuum (30 Pa) mode using the low-vacuum backscatter detector (LV-SEM−BSE). To prepare the samples for analysis, some were mounted in resin and cross-sectioned or cut with a razor. For the beads that were cut in half with a razor blade, the halves were mounted either cut side up or cut side down on top of carbon tape on aluminum stubs. The puck and the cut composite beads were coated with 2.5 nm of Pt using a sputter coater (EMS Quorum 150T ES). Images were postprocessed in Adobe Photoshop CC 2019 to adjust for charging artifacts and brightness interferences from detector shadowing.

Bead measurements were performed on optical micrographs of the beads. For each bead measured, both the minimum (i.e., short side) and maximum (i.e., long side) dimensions were measured for eight different beads. Averages were taken for all measurements of each sample as well as the averages of the short side and long side. Standard deviations (SD) were calculated as $\pm 1\sigma$.

2.4. X-ray Diffraction. A Bruker D8 ADVANCE (Bruker AXS Inc., Madison, WI) X-ray diffractometer (XRD) with Cu Kα emission

was used for capturing diffraction patterns of the as-made composites. The detector used was a LynxEye position-sensitive detector with a collection window of 3° 2θ. The activated HKUST-1 particles were added to the flat side of a zero-background quartz holder. The 90% HK composite beads were pressed into a flat disc using a pellet press and a 10 mm die and placed onto a zero-background quartz holder (32 mm diameter and 2.5 mm thick, MTI Corporation, Richmond, CA). Scan parameters were 5−50° 2θ with a step of 0.02° 2θ and 2 s dwell at each step for HKUST-1 with a step of 0.01° 2θ and 6 s dwell at each step for the 90%HK composite. Data were plotted in IGOR Pro (v8.0.3.3).

After the γ irradiation, XRD measurements for the irradiated composites were carried out using the PANalytical X'Pert Pro, which has a 1.8 kW sealed X-ray tube source, utilizing a Cu target, and a vertical circle θ with a radius of 240 mm. HighScore Plus software was employed to solve XRD data.

2.5. X-ray Computed Tomography. Single beads of MOF samples mounted onto the end of a plastic stick were imaged using X-ray computed tomography (XCT) on an X-Tek/Metris XTH 320/

225 kV scanner (Nikon Metrology, Belmont, CA). Data was collected at 55 kV and 400 μA X-ray power. The samples were rotated continuously during the scans with momentary stops to collect each projection (shuttling mode) while minimizing ring artifacts. A total of 3000 projections were collected over 360° rotation recording 4 frames per projection with a 708 ms exposure time per frame. The image voxel size was 3.2 μm. The images were reconstructed to obtain three-dimensional (3D) data sets using CT Pro 3D (Metris XT 2.2, Nikon Metrology). Representative slices and 3D images were acquired using VG Studio MAX 2.1 (Volume Graphics GmbH, Heidelberg, Germany).

2.6. Mechanical Stability. To demonstrate the mechanical stability of the engineered composites, a TA Instruments Q800 dynamic mechanical analyzer was used to investigate the mechanical properties of the MOF-based composites, including Young's modulus and strain at breaking. The testing was performed using a compression setup under the controlled force mode. A preloading force of 0.001 N, force track of 125%, and frequency of 1 Hz were adopted. Each sample was previously measured in diameter and mounted into fixtures by 5 in-lb torque force. Then, the sample was pressed at room temperature by ramping force at a rate of 0.5 N min^{-1} until breakage or 35% diameter of displacement was reached if it did not break, during which, stress and strain data were recorded. The stress is corrected with some assumptions where the material is assumed to be 100% compressible where the hoop diameter does not increase during compression. The contact area was estimated at each strain level and the force was divided by the contact area to get stress for each corresponding strain.

2.7. Xe Adsorption. To gain insights into the effect shaping had on xenon adsorption, we conducted adsorption experiments using a Quantachrome Autosorb IQ 2 instrument with the sample held at −80 °C. Samples were activated at 150 °C under vacuum at a rate of 5 °C min^{-1} for 12 h on the outgassing side of the instrument. The dry mass was measured, and the sample was cooled using a cryostat to the desired temperature. The pressure points were set beforehand using Quantachrome software. Volumetric changes, resulting from adsorption at each pressure step, were plotted against the pressure.

2.8. Specific Surface Area. Specific surface area (SSA) and pore structure were analyzed by $N_{2(g)}$ adsorption at 77 K with an automatic gas sorption system: QUADRASORB EVO/SI from Quantachrome Instruments (a brand of Anton Paar). The samples were degassed under vacuum at 150 °C for 15 h before the adsorption measurements. The surface area was determined using a 5-point Brunauer−Emmett−Teller (BET) method, and the Barrett−Joyner−Halenda (BJH) method was used for the pore volume and pore size distribution determination.

2.9. Density. MOF−PAN composite densities were measured using a Micromeritics AccuPyc II 1340 He gas pycnometer. Prior to running samples, the instrument volume was calibrated with a standard of known volume provided by the vendor. Sample masses were weighed on the ME204E analytical balance and then loaded into the pycnometer for 10 volume measurements, which, when combined with the mass measurements, were used to calculate densities.

2.10. γ Irradiation. The γ irradiation facility is an MIT Core User Facility managed by the MIT Radiation Protection Program (RPP) and houses a Gammacell 220 Excel self-shielded high-dose-rate γ-ray irradiator (Figure S3, Supporting Information). The irradiator was manufactured in Canada by MDS Nordion on 10/13/2003 and contained an initial quantity of cobalt-60 (Co-60) of 375.2 TBq (23,654 Ci) (Figure S4, Supporting Information). The current activity is 97.3 TBq (2630 Ci). The Co-60 sources are contained within a lead biological shield, which allows for the safe use of the irradiator by trained radiation workers.

The samples to be irradiated were loaded in the sample irradiation chamber and lowered by an elevator to the Co-60 source array (Figure S5, Supporting Information). The Co-60 sources are arranged in a caged array allowing for a uniform dose to the materials being irradiated (Figure S6, Supporting Information). The sample chamber is a thin-walled, closed, nonporous metal cylinder with a full-width door. The inside dimensions of the chamber are 15.49 cm diameter

and 20.47 cm height. The current chamber dose rate is 42.35 Gy min^{-1} (4235 Rads min^{-1}). The system can be operated in both an automatic and a manual mode. In the automatic mode, the user programs the timer for the total radiation dose required.

3. RESULTS AND DISCUSSION

The appearances of the as-made bead composites are shown in Figure 2a and b before and after drying, respectively. Before

Table 2. Summary of Average Composite Bead Sizes (in Millimeters) for Each Sample and for the Average of All Samples (Overall)[a]

sample	all measurements		short dimension		long dimension	
	ave.	SD	ave.	SD	ave.	SD
90%HK	3.28	0.21	3.22	0.20	3.34	0.21
75%HK	3.35	0.25	3.19	0.25	3.50	0.13
25%HK	3.07	0.19	2.96	0.17	3.18	0.15
10%HK	3.14	0.21	3.03	0.14	3.25	0.21
0%HK	3.02	0.31	2.93	0.25	3.11	0.36
overall	3.17	0.26				

[a]For each bead measured, both the minimum (i.e., short) and maximum (i.e., long) dimensions were measured for eight different beads. Standard deviations (SD) are ±1σ.

drying, the composites showed different shades of blue, and after drying, they appeared more purple, with the darkness of each color becoming higher with increased HKUST-1 loadings. The final beads have a narrow size distribution of 3.17 ± 0.26 mm (Table 2). The SSA values are provided in Table S1 and Figure S1 (Supporting Information) and show a trend with increasing SSA with added HKUST-1. A linear trendline fits well to the data if the 10%HK sample is omitted; a second-order polynomial fit aligns well to the full data set. The densities of the composites were observed to increase with increasing HKUST-1 loadings (see Table S2 and Figure S2, Supporting Information).

Figure 2c−m show images of various composites acquired from different techniques including optical microscopy (OM), SEM using backscattered electron (BSE) imaging, and XCT; these images reveal some critical details of these composites, some of which are the first of their kind. Figure 2c shows the activated HKUST-1 crystals, which are multifaceted and generally range from ∼30 to 70 μm in diameter. Figure 2d and e show whole-bead cross-sectional views of the 25%HK and 75%HK composites, respectively, taken using the Leica optical microscope. Since the resin is transparent, this is a great method for visualizing the distribution of the HKUST-1 crystals within the composites; it shows that the MOF is evenly distributed throughout both beads. These visualizations were not as meaningful for the 90%HK composites because the interior of the composite was packed tightly with the crystals, making light transmission difficult. Figure 2f shows the core of a cross-sectioned 90%HK composite bead, taken at a higher magnification using a Keyence VHX-2000 microscope. Figure 2g shows a higher-magnification SEM micrograph of the interior of a cut 75%HK composite, revealing the PAN pore network and embedded HKUST-1 crystals within the composite. Figure 2h−j shows progressively higher magnifications of the fibrous webbing of the PAN that comprises the composite structure, which allow these composites to work so well at allowing gases to flow through, while holding the MOFs in a stable configuration.
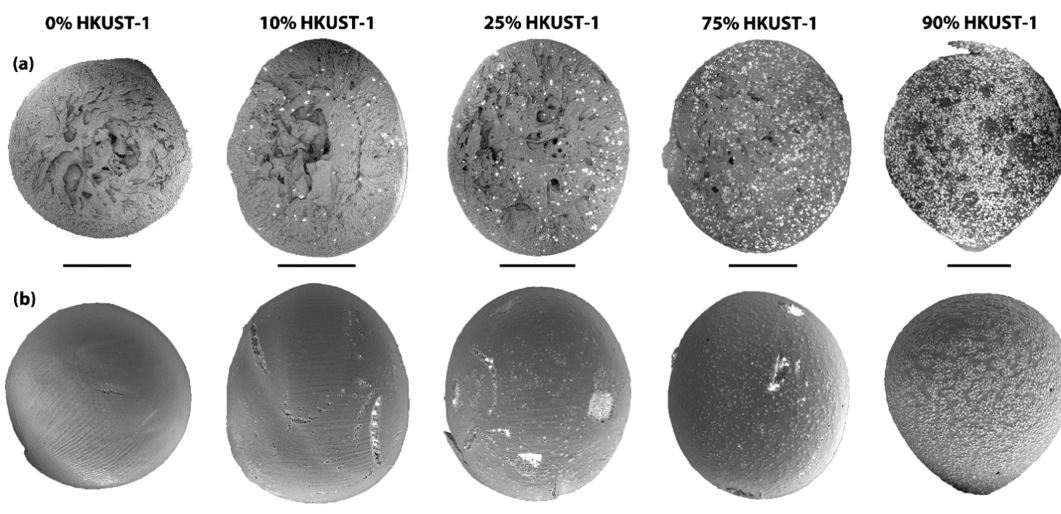
Figure 3. SEM micrographs of the (a) inside and (b) outside of the composites. The bright particles are crystals of the HKUST-1 MOF. The bars below each micrograph represent 1 mm.

Table 3. Summary of Mechanical Testing Experiments on the As-Made Composites and Composites Heat-Treated at 150 °C Prior to Testing[a]

sample ID	Young's modulus (MPa)	strain-to-failure (%)
0%HK	38.28	>35
75%HK	76.88	20.3
90%HK	165.6	13.74
0%HK-150 °C	147.6	>35
75%HK-150 °C	109.5	23.08
90%HK-150 °C	163.7	11.71

[a]Observations during the test include the following: 0%HK deformed only, 0%HK shrank 15% strain upon heating (deformed only), 75% HK and 90%HK both deformed and cracked, and 75%HK-150 °C and 90%HK-150 °C both collapsed and shattered.

Figure 4. Pictures of (a) 90%HK and (b) 90%HK-150 °C at the end of testing. (c) Mechanical testing results of the 0%HK, 75%HK, and 90%HK composites before and after the heat treatment at 150 °C; data for NUCON-activated carbon is also included in the plot for comparison.

Similarly, MOF−PAN composites were imaged using XCT to investigate the detailed microporosity of the engineered particles (Figure 2k−m). Visual inspection of the reconstructed three-dimensional data from XCT of pure PAN (Figure 2k), 75%HK (Figure 2l), and 90%HK (Figure 2m) composites shows that the pure PAN had the lowest density of the three samples, as expected based on the lack of added MOF, with significant porosity where most of the open pores were concentrated in the middle of the bead. The structure was composed of randomly oriented, but interconnected, layers or sheets of polymer. The 75%HK composite displayed a more heterogeneous distribution of the MOF as indicated by distinct regions of high-density (brighter) spots (Figure 2l). The porous microstructure of this sample can be described by the presence of large, 0.5−1 mm size, pores aggregated in the middle of the particle. The 90%HK composite showed an even more heterogeneous density distribution with a smaller average pore size, with the largest pore being ∼0.5 mm in size (Figure 2m).

The composite beads cross-sectioned with a razor and analyzed with low-magnification SEM are shown in Figure 3, which reveals a porous network within the composites. The PAN network was more difficult to visualize in this view at the higher HKUST-1 loadings within the composite beads. The HKUST-1 crystals are also more apparent along the exterior shell of 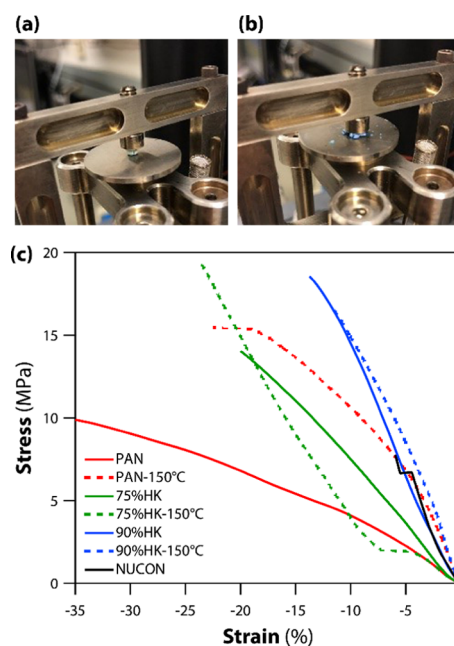the composites. In general, all of the composites appeared similar on the inner surfaces with small variations in pore sizes.

For mechanical stability testing, Young's modulus was calculated by taking the slope of the elastic region of the stress−strain curve (see Table 3). The ultimate compressive strength represents the highest stress in compression achieved prior to total failure or severe deformation. The term strain at breaking refers to the strain at which the sample breaks or deforms at least 35 vol %; these values are also presented in Table 3. A comparison of mechanical stability of the HKUST-1 MOF with and without the PAN binder in comparison with nuclear-grade activated carbon pellets indicates that MOF−PAN composites (Figure 4) have a superior mechanical stability than pristine MOF (not shown) and activated carbon
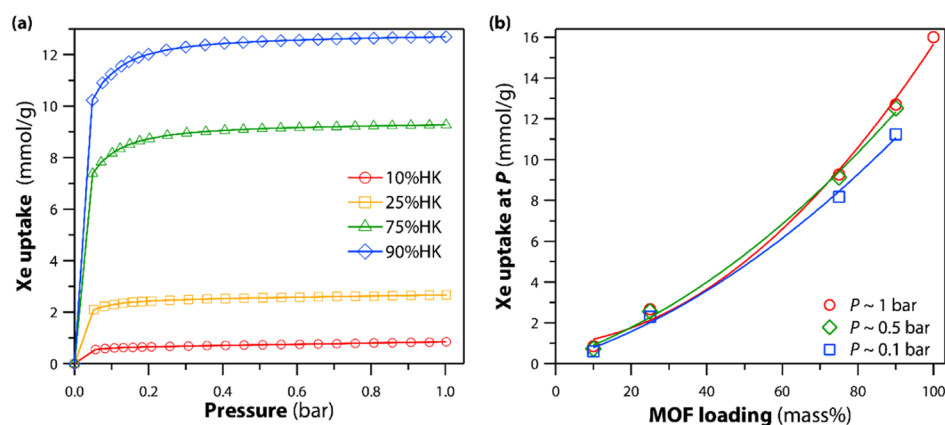
Figure 5. (a) Xe uptake at different pressures for different composites and (b) Xe uptake at ~0.1 bar, ~0.5 bar, and ~1 bar as a function of MOF (HKUST-1) loading in the composite; note that pure HKUST-1 (100% MOF loading) is included for comparison.
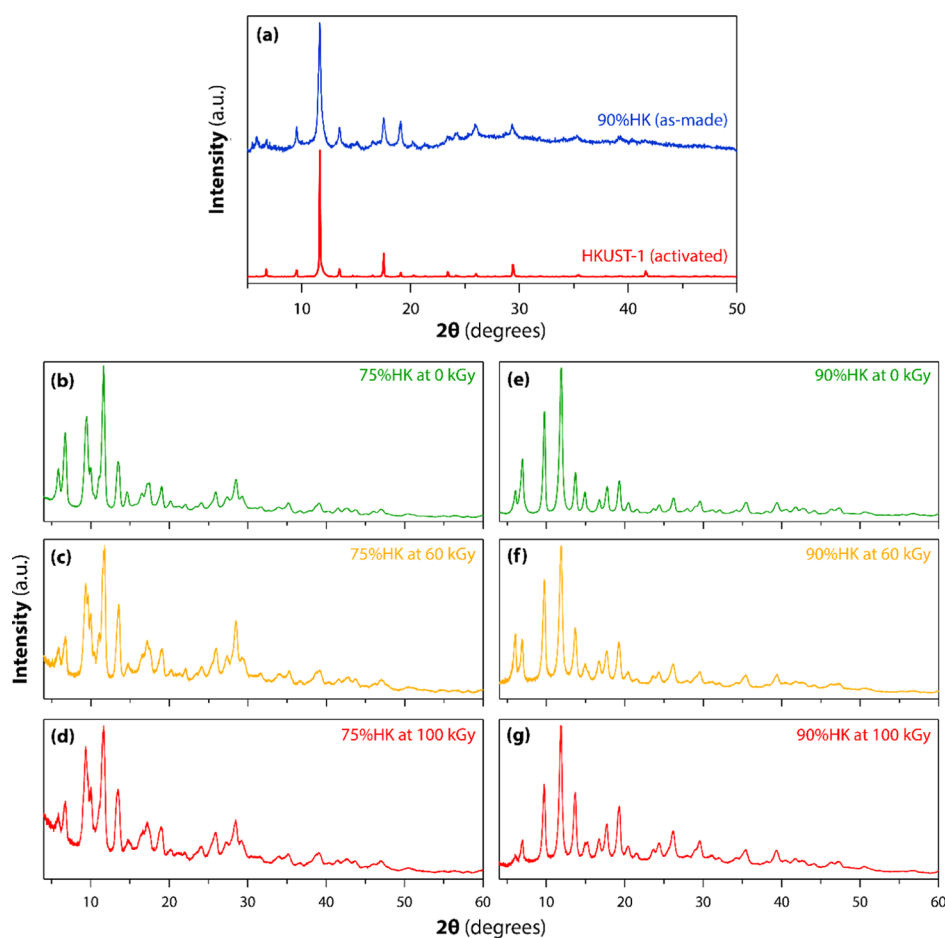

Figure 6. XRD summary of (a) 90%HK (as-made) and HKUST-1 (activated). (b−g) MOF−PAN composites (b, e) before and (c, d, f, g) after γ irradiations at (c, f) 60 kGy or (d, g) 100 kGy for (b−d) 75%HK and (e−g) 90%HK.

under identical conditions. The composites heat-treated at 150 °C showed improved crystallinity of PAN, so its modulus increased. Also, the discrepancy on the green dashed line in Figure 4c could be the result of the MOF getting compacted upon loading. It should also be noted that the pictures shown in Figure 4a and b reflect the appearances of 90%HK and 90%HK-150 °C after the testing. The 90%HK composite deformed under the load, and 90%HK-150 °C shattered into many pieces, demonstrating that the 150 °C heat treatment made the MOF−PAN composite brittle.

While HKUST-1 has already been documented as an effective Xe sorbent at low temperatures (−80 °C),[41] this is the first account showing MOFs as effective Xe sorbents while present in an engineered composite form. The Xe uptake is shown in Figure 5a for the composites. As shown in Figure 5a, an average 30% reduction in the capacity was observed over the total pressure range for the 90%HK composite, 50% reduction for the 75%HK composite, and 90% reduction for the 10%HK composite. This was expected, and the reduction in capacity can be attributed to the amount of PAN binder

used. Figure 5b shows a comparison of maximum uptake at 1 atm for each composite, and from this, it is apparent that the PAN matrix does not notably affect the Xe capture mechanism of the HKUST-1 MOF crystals. If successful, converting the MOF powders into shaped bodies would provide a clear path for large-scale implementation of these materials. The PAN binders show improved mechanical stability with minimal reduction in capacity (90%HK composite) at −80 °C using single-component gas adsorption isotherms. We are currently investigating the relationship between the amount of binder used and associated adsorption properties including single-column breakthrough experiments.

X-ray diffraction was used to evaluate the structure of the composites for comparison with the activated HKUST-1 crystals. Due to the high porosity and low interaction volumes of the porous composite beads, the 90%HK composite beads were used to maximize the diffraction intensities, and these were flattened using a pellet press to make them as thin as possible and reduce sample displacement from the diffraction plane. The data for both the activated HKUST-1 and 90%HK composite are provided in Figure 6a and show relatively good agreement between the diffraction peaks, with some preferred orientation. Also, the diffraction peak for the 90%HK composite shows a broad amorphous hump from ∼25 to 50° 2θ, which is presumably from the PAN composite network. Considering the excellent performance of the 90%HK and 75% HK composites for capturing Xe with superior affinity, it was important to investigate the effects of ionizing radiation on the stability of these structures. The quantitative analysis of the XRD data after irradiating the samples at 60 and 100 kGy is provided in Figure 6c,d,f,g and shows no apparent crystal or structural deformation. This demonstrates that the 90%HK and 75%HK composites have good radiation resistance (up to these fluxes) toward ionizing radiation and could potentially to be used for removing Xe off-gases during spent nuclear fuel treatment.

4. SUMMARY AND CONCLUSIONS

In summary, this study demonstrated the successful incorporation of HKUST-1 MOF crystals into a porous polyacrylonitrile matrix. The PAN matrix provides a rigid net that holds the crystals in place for the capture of gaseous Xe. The addition of MOF to the PAN matrix was demonstrated up to 90 mass % MOF (10 mass % PAN). The Xe capacity was observed to scale somewhat linearly with the MOF loading, providing evidence that the PAN matrix remains mostly passive to the Xe capture mechanism.

More work is needed to fully evaluate this technology for the HKUST-1 MOF. Additionally, this process should be evaluated for other MOFs. One of the main drawbacks to this method for MOFs is that the process described herein utilizes water as a PAN precipitation medium and many MOFs are sensitive to, or even incompatible with, water. Therefore, other solvent systems should be explored for applicability toward making MOF−PAN composites. Finally, MOFs have a wide range of applications, using this approach for capturing other hazardous materials should be evaluated.

ASSOCIATED CONTENT

Ⓢ Supporting Information

The Supporting Information is available free of charge at https://pubs.acs.org/doi/10.1021/acsami.0c13717.

Surface area and density of the HKUST-1 MOF−PAN beads presented along with radiation facility at MIT; density data for MOF-PAN composites as well as pure HKUST-1 and 100% PAN beads; and figures showing a Gammacell 220 Excel irradiator, original activity and weight, cutaway of Gammacell 220, and a Co-60 source array (PDF)

AUTHOR INFORMATION

Corresponding Author

Praveen K. Thallapally − *Pacific Northwest National Laboratory, Richland, Washington 99354, United States;* ⓞ orcid.org/0000-0001-7814-4467; Email: praveen.thallapally@pnnl.gov

Authors

Brian J. Riley − *Pacific Northwest National Laboratory, Richland, Washington 99354, United States;* ⓞ orcid.org/0000-0002-7745-6730

Saehwa Chong − *Pacific Northwest National Laboratory, Richland, Washington 99354, United States*

Wenbin Kuang − *Pacific Northwest National Laboratory, Richland, Washington 99354, United States*

Tamas Varga − *Pacific Northwest National Laboratory, Richland, Washington 99354, United States;* ⓞ orcid.org/0000-0002-5492-866X

Ahmed S. Helal − *Department of Nuclear Science and Engineering and Department of Materials Science and Engineering, Massachusetts Institute of Technology, Cambridge, Massachusetts 02139, United States*

Mitchell Galanek − *Office of Environment, Health & Safety, Massachusetts Institute of Technology, Cambridge, Massachusetts 02139, United States*

Ju Li − *Department of Nuclear Science and Engineering and Department of Materials Science and Engineering, Massachusetts Institute of Technology, Cambridge, Massachusetts 02139, United States;* ⓞ orcid.org/0000-0002-7841-8058

Zayne J. Nelson − *Pacific Northwest National Laboratory, Richland, Washington 99354, United States*

Complete contact information is available at:
https://pubs.acs.org/10.1021/acsami.0c13717

Notes

The authors declare no competing financial interest.

the composite production process. All authors contributed equally to this work.

■ REFERENCES

(1) Soelberg, N. R.; Garn, T. G.; Greenhalgh, M. R.; Law, J. D.; Jubin, R.; Strachan, D. M.; Thallapally, P. K. Radioactive Iodine and Krypton Control for Nuclear Fuel Reprocessing Facilities. *Sci. Technol. Nucl. Install.* **2013**, *2013*, No. 702496.

(2) Bruffey, S. H.; Jubin, R. T. Analysis of Krypton-85 Legacy Waste Forms: Part I. *Nucl. Technol.* **2017**, *200*, 159−169.

(3) Jubin, R. T.; Bruffey, S. H. Analysis of Krypton-85 Legacy Waste Forms: Part II. *Nucl. Technol.* **2019**, *205*, 830−846.

(4) Ludlow, J. A.; Lee, T. G. Investigating the static dipole polarizability of noble-gas atoms confined in impenetrable spheres and shells. *Phys. Rev. A* **2015**, *91*, No. 032507.

(5) Banerjee, D.; Simon, C. M.; Elsaidi, S. K.; Haranczyk, M.; Thallapally, P. K. Xenon Gas Separation and Storage Using Metal-Organic Frameworks. *Chem* **2018**, *4*, 466−494.

(6) Thomas, V. C.; Makowski, J. M.; Brown, G. M.; McCarthy, J. F.; Bruno, D.; Cardoso, J. C.; Chiville, W. M.; Meyer, T. F.; Nelson, K. E.; Pavri, B. E.; Termohlen, D. A.; Violet, M. D.; Williams, J. B. The Dawn Spacecraft. *Space Sci. Rev.* **2011**, *163*, 175−249.

(7) Kennedy, R. R.; Stokes, J. W.; Downing, P. Anesthesia and the Inert-Gases with Special Reference to Xenon. *Anaesth. Intensive Care* **1992**, *20*, 66−70.

(8) Claude, G. On the air treatment with a view to extracting krypton and xenon from it, and on the application of these gases to incandescent lamps. *Cr. Hebd. Acad. Sci.* **1934**, *198*, 1959−1962.

(9) Collard, G.; Goossens, W. R. A.; Vaesen, J.; Glibert, R.; Baetsle, L. H. Cryogenic Distillation Unit for Krypton and Xenon Removal from Gaseous Effluents. *Trans. Am. Nucl. Soc.* **1979**, *31*, 514−516.

(10) Banerjee, D.; Simon, C. M.; Plonka, A. M.; Motkuri, R. K.; Liu, J.; Chen, X.; Smit, B.; Parise, J. B.; Haranczyk, M.; Thallapally, P. K. Metal-organic framework with optimally selective xenon adsorption and separation. *Nat. Commun.* **2016**, *7*, No. ncomms11831.

(11) Wu, T.; Feng, X. H.; Elsaidi, S. K.; Thallapally, P. K.; Carreon, M. A. Zeolitic Imidazolate Framework-8 (ZIF-8) Membranes for Kr/Xe Separation. *Ind. Eng. Chem. Res.* **2017**, *56*, 1682−1686.

(12) Wu, T.; Lucero, J.; Zong, Z. W.; Elsaidi, S. K.; Thallapally, P. K.; Carreon, M. A. Microporous Crystalline Membranes for Kr/Xe Separation: Comparison Between AlPO-18, SAPO-34, and ZIF-8. *ACS Appl. Nano Mater.* **2018**, *1*, 463−470.

(13) Matsuda, R.; Kitaura, R.; Kitagawa, S.; Kubota, Y.; Belosludov, R. V.; Kobayashi, T. C.; Sakamoto, H.; Chiba, T.; Takata, M.; Kawazoe, Y.; Mita, Y. Highly controlled acetylene accommodation in a metal-organic microporous material. *Nature* **2005**, *436*, 238−241.

(14) Yaghi, O. M.; O'Keeffe, M.; Ockwig, N. W.; Chae, H. K.; Eddaoudi, M.; Kim, J. Reticular synthesis and the design of new materials. *Nature* **2003**, *423*, 705−714.

(15) Perry, J. J.; Teich-McGoldrick, S. L.; Meek, S. T.; Greathouse, J. A.; Haranczyk, M.; Allendorf, M. D. Noble Gas Adsorption in Metal-Organic Frameworks Containing Open Metal Sites. *J. Phys. Chem. C* **2014**, *118*, 11685−11698.

(16) Liu, J.; Strachan, D. M.; Thallapally, P. K. Enhanced noble gas adsorption in Ag@MOF-74Ni. *Chem. Commun.* **2014**, *50*, 466−468.

(17) Kapelewski, M. T.; Oktawiec, J.; Runcevski, T.; Gonzalez, M. I.; Long, J. R. Separation of Xenon and Krypton in the Metal-Organic Frameworks M-2(m-dobdc) (M = Co, Ni). *Isr. J. Chem.* **2018**, *58*, 1138−1143.

(18) Lee, S. J.; Kim, K. C.; Yoon, T. U.; Kim, M. B.; Bae, Y. S. Selective dynamic separation of Xe and Kr in Co-MOF-74 through strong binding strength between Xe atom and unsaturated Co^{2+} site. *Microporous Mesoporous Mater.* **2016**, *236*, 284−291.

(19) Meek, S. T.; Teich-McGoldrick, S. L.; Perry, J. J.; Greathouse, J. A.; Allendorf, M. D. Effects of Polarizability on the Adsorption of Noble Gases at Low Pressures in Monohalogenated Isoreticular Metal-Organic Frameworks. *J. Phys. Chem. C* **2012**, *116*, 19765−19772.

(20) Thallapally, P. K.; Grate, J. W.; Motkuri, R. K. Facile xenon capture and release at room temperature using a metal-organic framework: a comparison with activated charcoal. *Chem. Commun.* **2012**, *48*, 347−349.

(21) Fernandez, C. A.; Liu, J.; Thallapally, P. K.; Strachan, D. M. Switching Kr/Xe Selectivity with Temperature in a Metal-Organic Framework. *J. Am. Chem. Soc.* **2012**, *134*, 9046−9049.

(22) Idrees, K. B.; Chen, Z. J.; Zhang, X.; Mian, M. R.; Drout, R. J.; Islamoglu, T.; Farha, O. K. Tailoring Pore Aperture and Structural Defects in Zirconium-Based Metal-Organic Frameworks for Krypton/Xenon Separation. *Chem. Mater.* **2020**, *32*, 3776−3782.

(23) Li, L. Y.; Guo, L. D.; Zhang, Z. G.; Yang, Q. W.; Yang, Y. W.; Bao, Z.; Ren, Q. L.; Li, J. A Robust Squarate-Based Metal-Organic Framework Demonstrates Record-High Affinity and Selectivity for Xenon over Krypton. *J. Am. Chem. Soc.* **2019**, *141*, 9358−9364.

(24) Chen, X. Y.; Plonka, A. M.; Banerjee, D.; Krishna, R.; Schaef, H. T.; Ghose, S.; Thallapally, P. K.; Parise, J. B. Direct Observation of Xe and Kr Adsorption in a Xe-Selective Microporous Metal-Organic Framework. *J. Am. Chem. Soc.* **2015**, *137*, 7007−7010.

(25) Banerjee, D.; Elsaidi, S. K.; Thallapally, P. K. Xe adsorption and separation properties of a series of microporous metal-organic frameworks (MOFs) with V-shaped linkers. *J. Mater. Chem. A* **2017**, *5*, 16611−16615.

(26) Li, J. L.; Huang, L.; Zou, X. Q.; Zheng, A. M.; Li, H. Y.; Rong, H. Z.; Zhu, G. S. Porous organic materials with ultra-small pores and sulfonic functionality for xenon capture with exceptional selectivity. *J. Mater. Chem. A* **2018**, *6*, 11163−11168.

(27) Xiong, S. S.; Liu, Q.; Wang, Q.; Li, W.; Tang, Y. M.; Wang, X. L.; Hu, S.; Chen, B. L. A flexible zinc tetrazolate framework exhibiting breathing behaviour on xenon adsorption and selective adsorption of xenon over other noble gases. *J. Mater. Chem. A* **2015**, *3*, 10747−10752.

(28) Liu, J.; Thallapally, P. K.; Strachan, D. Metal-Organic Frameworks for Removal of Xe and Kr from Nuclear Fuel Reprocessing Plants. *Langmuir* **2012**, *28*, 11584−11589.

(29) Liu, J.; Fernandez, C. A.; Martin, P. F.; Thallapally, P. K.; Strachan, D. M. A Two-Column Method for the Separation of Kr and Xe from Process Off-Gases. *Ind. Eng. Chem. Res.* **2014**, *53*, 12893−12899.

(30) Chen, L.; Reiss, P. S.; Chong, S. Y.; Holden, D.; Jelfs, K. E.; Hasell, T.; Little, M. A.; Kewley, A.; Briggs, M. E.; Stephenson, A.; Thomas, K. M.; Armstrong, J. A.; Bell, J.; Busto, J.; Noel, R.; Liu, J.; Strachan, D. M.; Thallapally, P. K.; Cooper, A. I. Separation of rare gases and chiral molecules by selective binding in porous organic cages. *Nat. Mater.* **2014**, *13*, 954−960.

(31) Ladshaw, A. P.; Wiechert, A. I.; Welty, A. K.; Lyon, K. L.; Law, J. D.; Jubin, R. T.; Tsouris, C.; Yiacoumi, S. Adsorbents and adsorption models for capture of Kr and Xe gas mixtures in fixed-bed columns. *Chem. Eng. J.* **2019**, *375*, No. 122073.

(32) Sikora, B. J.; Wilmer, C. E.; Greenfield, M. L.; Snurr, R. Q. Thermodynamic analysis of Xe/Kr selectivity in over 137 000 hypothetical metal-organic frameworks. *Chem. Sci.* **2012**, *3*, 2217−2223.

(33) Van Heest, T.; Teich-McGoldrick, S. L.; Greathouse, J. A.; Allendorf, M. D.; Sholl, D. S. Identification of Metal-Organic Framework Materials for Adsorption Separation of Rare Gases: Applicability of Ideal Adsorbed Solution Theory (IAST) and Effects of Inaccessible Framework Regions. *J. Phys. Chem. C* **2012**, *116*, 13183−13195.

(34) Sumer, Z.; Keskin, S. Molecular simulations of MOF adsorbents and membranes for noble gas separations. *Chem. Eng. Sci.* **2017**, *164*, 108−121.

(35) Simon, C. M.; Mercado, R.; Schnell, S. K.; Smit, B.; Haranczyk, M. What Are the Best Materials To Separate a Xenon/Krypton Mixture? *Chem. Mater.* **2015**, *27*, 4459−4475.

(36) Kalaj, M.; Cohen, S. M. Spray-Coating of Catalytically Active MOF-Polythiourea through Postsynthetic Polymerization. *Angew. Chem., Int. Ed.* **2020**, *59*, 13984−13989.

(37) Semino, R.; Moreton, J. C.; Ramsahye, N. A.; Cohen, S. M.; Maurin, G. Understanding the origins of metal-organic framework/polymer compatibility. *Chem. Sci.* **2018**, *9*, 315−324.

(38) Garzón-Tovar, L.; Cano-Sarabia, M.; Carne-Sanchez, A.; Carbonell, C.; Imaz, I.; Maspoch, D. A spray-drying continuous-flow method for simultaneous synthesis and shaping of microspherical high nuclearity MOF beads. *React. Chem. Eng.* **2016**, *1*, 533−539.

(39) Riley, B. J.; Pierce, D. A.; Chun, J.; Matyáš, J.; Lepry, W. C.; Garn, T.; Law, J.; Kanatzidis, M. G. Polyacrylonitrile-chalcogel hybrid sorbents for radioiodine capture. *Environ. Sci. Technol.* **2014**, *48*, 5832−5839.

(40) Riley, B. J.; Garn, T. Purification of Gas and Liquid Streams Using Composite Sorbents Embedded in a Polyacrylonitrile Matrix. *Advances in Materials Science Research*;Wythers, M., Ed.; Nova Science Publishers, 2019; 35, pp 119−147.

(41) Elsaidi, S. K.; Ongari, D.; Xu, W. Q.; Mohamed, M. H.; Haranczyk, M.; Thallapally, P. K. Xenon Recovery at Room Temperature using Metal-Organic Frameworks. *Chem. - Eur. J.* **2017**, *23*, 10758−10762.

Supporting Information

Metal-organic framework-polyacrylonitrile composite beads for xenon capture

Brian J. Riley,[a] Saehwa Chong,[a] Wenbin Kuang,[a] Tamas Varga,[a] Ahmed S. Helal,[b]

Mitchell Galanek,[c] Ju Li,[b] and Zayne J. Nelson[a] Praveen K. Thallapally,*,[a]

[a]Pacific Northwest National Laboratory, 902 Battelle Blvd, Richland, WA 99354, USA

[b]Department of Nuclear Science and Engineering and Department of Materials Science and

Engineering, Massachusetts Institute of Technology, Cambridge, MA 02139, USA

[c]Office of Environment, Health & Safety, Massachusetts Institute of Technology, Cambridge, MA 02139, USA

E-mail: praveen.thallapally@pnnl.gov

Supporting Information

1   Specific Surface Area

The data from these measurements are shown in Table S1 and plotted in Figure S1 as a function of MOF (HKUST-1) loading.

Table S1. Summary of BET specific surface area (*SSA*) and micropore surface area (*MSA*) measured using the T method. The 100%HK sample is the pure HKUST-1 MOF.

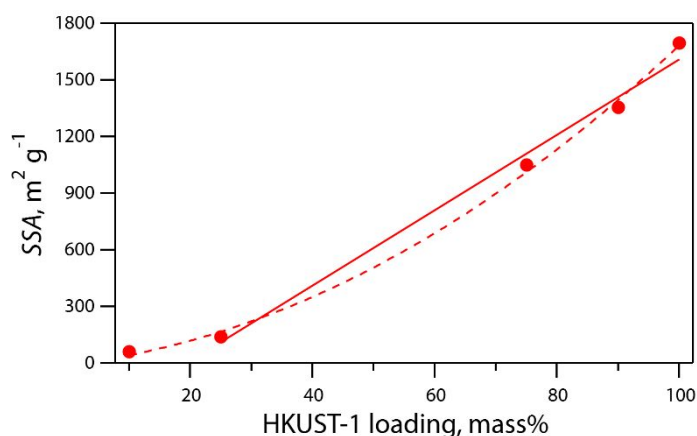| Sample	*SSA* (m^2 g^{-1})	*MSA* (m^2 g^{-1})
10%HK	60	–
25%HK	140	–
75%HK	1051	879
90%HK	1355	1183
100%HK	1695	–

Figure S1. *SSA* as a function of HKUST-1 (MOF) loading in the composites; included is the pure HKUST-1 MOF. Both 2nd-order polynomial (all data) and linear (without 10%HK) fits are shown.

2   Density

The density values provided in Table S2 are the averages and standard deviations of these measurements.

Table S2. Density data for MOF-PAN composites as well as pure HKUST-1 and 100% PAN beads. Here, HK is the mass loading of HKUST-1 MOF in the sample and "STDEV" is the standard deviation (±1σ).

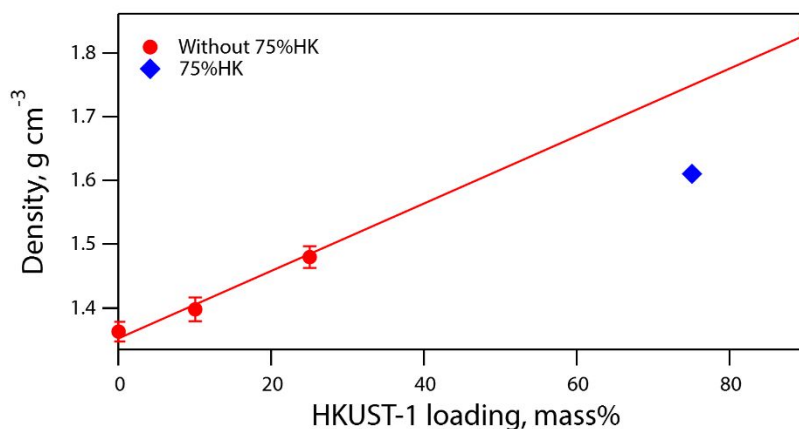| Sample	HK (mass%)	ρ (g cm^{-3})	STDEV (g cm^{-3})
90%HK	90	1.8314	0.0178
75%HK	75	1.6112	0.0032
25%HK	25	1.4800	0.0171
10%HK	10	1.3980	0.0190
0%HK (pure PAN)	0	1.3631	0.0158

Figure S2. Summary of density data for MOF-PAN composites.

3 Radiation Safety

All research groups requiring of the MIT gamma irradiation facility must have their projects registered and approved by the MIT Radiation Protection Committee. Individual users must complete an online Gammacell specific radiation safety course accompanied by site specific training including hands-on instruction on the use of the system as well as security and emergency response training. Annual retraining is required for all users. All users are monitored for potential radiation exposure and required to wear radiation dosimetry when using the irradiation facility.

4 Security

The irradiator facility has an extensive access control and security system. MIT Police and Operations Center monitor security and radiation alarms continuously (24 h day^{-1}). Only trained radiation workers who have been qualified as trustworthy and reliable can gain unescorted access to use the facilities.

Figure S3. Gammacell 220 Excel Irradiator.

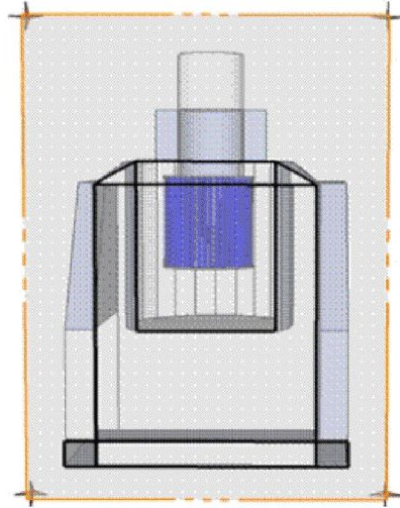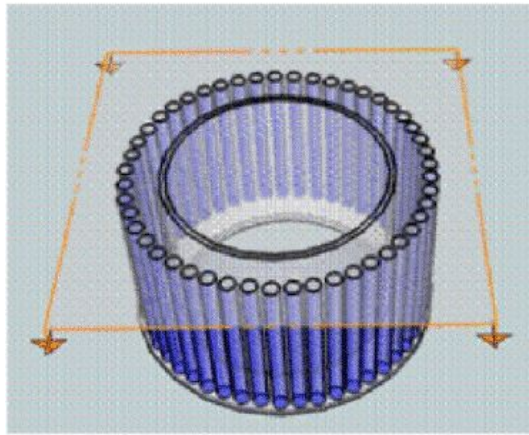**Figure S4. Original Activity and Weight.**

Figure S5. Cutaway of Gammacell 220.

Figure S6. Co-60 source array.